RSC Advances

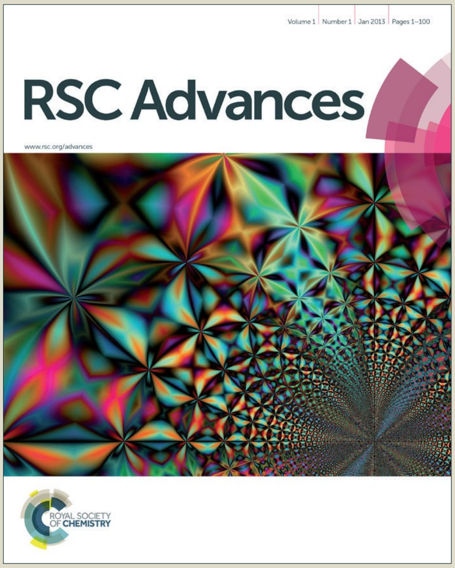

ROYAL SOCIETY OF CHEMISTRY

www.rsc.org/advances

Electronic properties and photoactivity of monolayer MoS_2/fullerene van der Waals heterostructures

Cai-Yun Luo[1], Wei-Qing Huang[1*], Liang Xu[2, 1], Yin-Cai Yang[1], Xiaofan Li[1$], Wangyu Hu[2], P. Peng[2], Gui-Fang Huang[1#]

[1] Department of Applied Physics, School of Physics and Electronics, Hunan University, Changsha 410082, China

[2] School of Materials Science and Engineering, Hunan University, Changsha 410082, China

Abstract: Van der Waals (vdW) heterostructures have attracted immense interest recently due to their unusual properties and new phenomena. Atomically thin two-dimensional MoS_2 heterostructures are particularly exciting for novel photovoltaic applications, because monolayer MoS_2 has a band gap in the visible spectral range and exhibit extremely strong light–matter interactions. Herein, first-principles calculations based on density functional theory is used to investigate the effects of vdW interactions on changes in the electronic structure, charge transfer and photoactivity in three typical monolayer MoS_2/fullerene (C_{60}, C_{26}, and C_{20}) heterostructures. Compared to monolayer MoS_2, the band gap of the heterostructures is smaller, which can enhance the visible light absorption and photoinduced electrons transfer. The amount of charge transfer at interface induced by vdW interaction depends on the size of fullerenes. Most importantly, a type-II, staggered band alignment can be obtained in the MoS_2/C_{20} heterostructure, leading to significantly reduced charge recombination and thus enhanced photocatalytic activity. These results reveal that fullerene modification would be an effective strategy to improve the photocatalytic performance of semiconductor photocatalysts.

Keywords: Monolayer MoS_2; Fullerene; Heterostructures; Photocatalytic activity; First-Principles calculations

---

*. Corresponding author. *E-mail addresses:* wqhuang@hnu.edu.cn

$. Corresponding author. *E-mail:* yueyanglxf@hnu.edu.cn

#. Corresponding author. *E-mail address:* gfhuang@hnu.edu.cn

1. Introduction

Semiconductor photocatalytic technology has attracted considerable attention due to its great potential in solving current environment and energy problems with abundant solar light [1-3]. To date, various kinds of semiconductor photocatalysts including metal oxides, sulfides and nitrides have been explored [4, 5]. However, the development of efficient, sustainable, visible (vis-) light-driven photocatalysts remains a significant challenge. For example, TiO_2, as a paradigm photocatalyst, is a large-band-gap semiconductor (~3.2 eV) [5], only showing photocatalytic activity under ultraviolet (UV-) irradiation. Therefore, the pursuit of photocatalysts with high performance under vis-light irradiation would be very desirable [4, 6].

In recent years, the use of carbonaceous materials such as fullerene, carbon nanotubes (CNTs) and graphene (GR) for the enhancement of photocatalytic performances of semiconductors has been demonstrated because of their special structures and unique electronic properties [7, 8]. Many novel heterojunction photocatalysts by combination of C_3N_4 with carbonaceous materials have been explored. For instance, the graphene/C_3N_4 heterostructures, prepared by the impregnation–chemical reduction strategy, show high vis-light photocatalytic activity for hydrogen production [9]. Graphene, CNTs and fullerene have also been used to interface with TiO_2 to achieve extended photocatalytic activities well beyond that of pure TiO_2 materials [10]. The enhanced photocatalytic performance of semiconductor/carbon heterostructures is generally attributed to the electron-accepting and transport properties of carbon nanomaterials since they provide a convenient way to direct the flow of photogenerated charge carriers [11, 12].

Density functional theory (DFT) has been used to reveal the underlying mechanisms for superior photocatalytic performance of semiconductor/carbons nanomaterials. It has been demonstrated that coupling carbon nanomaterials can reduce the band gap of semiconductors, thus enhancing optical absorption in the visible region [13]. It is found that graphene is the sensitizer for TiO_2 [14]and g-C_3N_4 [15], whereas significant charges transfer from anatase TiO_2 to graphene at the ground electronic state is also revealed due to the different crystal structure. The simulations by long et al. rationalized the photocatalytic activity of CNT/TiO_2 heterostructures materials under vis-light is higher than UV-irradiation, and showed that the photoactivity of a semiconducting CNT decorating TiO_2 is better than that of the metallic CNT/TiO_2 heterostructures [10, 16, 17]. The

DFT calculations also suggest that C_{60}-interfaced TiO_2 in both the mechanical mixture and covalent linking cannot form an efficient photovoltaic heterojunction [18]. Whereas B- or N-doped C_{60} and MoS_2 or WS_2 monolayers can form an efficient photovoltaic heterojunctions [19].

Over the last few years, aroused by the discovery of graphene, two-dimensional (2D) nanomaterials have been largely researched in the field of industrial and scientific for their unique properties and wide potential applications [11]. Recently, there has been a continual growth in research and a broad interest in monolayer MoS_2, which has a similar structure to grapheme [20, 21]. The monolayer MoS_2 consists of molybdenum atoms sandwiched between two layers of hexagonally close packed sulfur atoms, that the adjacent atomic sandwiches are held together by weakly vdW forces [22, 23], which have become particularly interesting due to their enhanced structural complexity and the potential to exploit the functionalities of these nanomaterials, making it a up-and-coming candidate for many useful applications, such as outstanding photoluminescence[24], lithium battery cathodes, sensors, phototransistor and photocatalytic hydrogen production applications [25]. However, photocatalytic and field emission abilities of MoS_2 are not productive enough for large scale applications in industry because of the relatively sizable band gaps (1.9 eV), a rapid recombination rate of photogenerated electrons and holes and lacking of effective emission sites [26]. Nevertheless, lots of previous studies revealed the fact that forming hetero-nanostructure can give the nanomaterials a better performance in electronics, optoelectronics and other aspects because of the generation of hetero-junction, enlarged specific surface area and so on, such as MoS_2/CdS [27], MoS_2/TiO_2 [28], MoS_2/SnO_2 [29] and MoS_2/Ag_3PO_4 [30].

More recently, MoS_2/carbon-nanomaterials heterostructures have been attracting increasing attention due to their highly efficient vis-light photocatalytic performances. For instance, the MoS_2/graphene heterostructures prepared by different methods show superior vis-light-driven photocatalytic activity [20]. Similarly, Yu and coworkers reported that TiO_2 grown on layered MoS_2/graphene heterostructures showed an enhanced photocatalytic H_2 evolution activity [31]. It is also found that MoS_2/CNT heterostructures exhibits high catalytic activity for electrocatalytic hydrogen evolution [32]. Compared with graphene and CNTs, fullerene have been attracted paritcular interest owing to their functional characteristics and potential applications in the fields of nanomaterials and biomedical science [33]. Therefore, it is expected to improve the photocatalytic performance of MoS_2 by fullerene modification, just as the case of C_{60}/TiO_2 [34].

In this work, the structural and electronic properties of monolayer MoS_2/fullerene vdW heterostructures have been investigated using large-scale DFT computations to explore the effects of non-covalent interactions on enhancing the photoactivity of monolayer MoS_2 by fullerene modification. Here, $C_{60,}$ C_{26} and C_{20} are taken as the typical fullerenes, motivated by their special structure and properties [35, 36]. The fullerene C_{60} is a closed-shell configuration consisting of 30 bonding molecular orbitals with 60 π-electrons, which is favorable for efficient electron transfer reduction [37]; C_{20} consisting solely of pentagons, is the smallest unconventional fullerene which breaks the ‘‘isolated pentagon rule” [38], while fullerene C_{26} is pure and intermediate open-shell compound [39]. Moreover, these fullerenes are well established as single oxygen sensitizers for electron donor-acceptor assemblies and applies in the field of photocatalysis [7, 11, 40]. Most importantly, Remskar M. et al. have successfully prepared hybrid MoS_2/C_{60} crystals, and found that the inherent close proximity of photovoltaic-active MoS_2 monolayers to C_{60} molecules with strong electron affinities suggests a new kind of material for solar-cell applications with high quantum yields of photoinduced charge generation [41]. The role of fullerene in these photocatalytic systems can be speculated to be as follows: (1) it can form the space potential difference promoting the photogenerated electron-hole separation effectively; (2) it can tune the band gap by changing the band structure of the photocatalysts. The calculated results showed that the band gap can be largely reduced due to interfacing with fullerene, resulting into a strong absorption in the entire visible region and thus superior photocatalytic activity. The electrostatic potential distribution in the interface, where the potential at MoS_2 is higher than that in fullerene, can effectively inhibit the electron-hole pair’s recombination and therefore improving its photocatalytic. This work would provide some new insight into optimizing the photocatalytic properties of MoS_2-based or carbon-based nanomaterial heterostructures.

2. Computational Method

All of our calculations, including geometry relaxation and electronic structure calculation are performed by using DFT method implemented in the plane wave basis CASTEP code [42, 43]. The local density approximation (LDA) with inclusion of the vdW interaction is chosen because long-range vdW interactions are expected to be significant in such these complexes. The cutoff energy for plane waves is chosen to be 400 eV. A Monkhorst-Pack mesh of k points, 2 × 2 × 1 and 4 × 4 × 1 points, is used, respectively, to sample the two-dimensional Brillouin zone for geometry optimization and for calculating the density of states, and the convergence tolerance of force on each atom during structure relaxation is set at 0.01 eV/Å [44].

For the monolayer MoS_2, the calculated lattice constant is in good agreement with the previous theoretical results[45]. The monolayer MoS_2/fullerene vdW heterostructures are composited by using a supercell as illustrated in Fig. 1. The supercell ($18.69 \times 18.69 \times 25.00$ Å^3) contains C_{60}, C_{26}, C_{20} (containing 60, 26, and 20 atoms, respectively) and one 6×6 monolayer MoS_2 (containing 36 Mo and 72 S atoms). A vacuum layer of 15 Å is used in the direction normal to the interface, representing the isolated slab boundary condition. Note that there is no tensile or compressed deformation of MoS_2 surface in the *x-y* plane, different from other models (CeO_2/GR [46], MoS_2/GR [20], g-C_3N_4/GR [9], TiO_2/CNT [10], $SrTiO_3$/GR [47]).

The strong light absorption is one of fundamental premises for a high-efficiency photocatalyst. The dielectric function of the semiconductor materials is mainly connected with the electronic response. The frequency-dependent dielectric matrix is calculated for pure MoS_2, and MoS_2/fullerene (C_{60}, C_{26}, and C_{20}) heterostructures by the Fermi golden rule within the dipole approximation. The imaginary part ε_2 of the dielectric function ε is calculated from the momentum matrix elements between the occupied and unoccupied wave functions, as given by:

$$\varepsilon_2 = \frac{ve^2}{2\pi\hbar m^2\omega^2}\int d^3k \sum_{n,n'} |\langle kn|p|kn'\rangle|^2 f(kn)(1-f(kn'))\delta(E_{kn}-E_{kn'}-\hbar\omega) \qquad (1)$$

where $\hbar\varpi$ is the energy of the incident photon, p is the momentum operator $r(\hbar/i)(\partial/\partial x)$, $(|kn\rangle)$ is a crystal wave function and $f(kn)$ is Fermi function. The real part ε_1 of the dielectric function ε is evaluated from the imaginary part ε_2 by Kramer–Kronig transformation. The absorption coefficient $I(\varpi)$ can be derived from ε_1 and ε_2, as given by:

$$I(\varpi) = \sqrt{2}\varpi\left[\sqrt{\varepsilon_1^2(\varpi) + \varepsilon_2^2(\varpi)} - \varepsilon_1(\varpi)\right]^{1/2} \quad (2)$$

which depends on ε_1 and ε_2 and thus on the energy. Taking into account the tensor nature of the dielectric function, ε_1 (ω) and ε_2 (ω) are averaged over three polarization vectors (along x, y, and z directions). All other optical constants can also be obtained. The relations above are the theoretical basis of band structure and optical properties analyzing which reflected the mechanism of absorption spectral caused by electronic transition between different energy levels.

3. Results and Discussion

3.1. Geometric Structure and Adhesion Energy

Figure 1(a-d) show the fully optimized geometric structures of the monolayer MoS_2/fullerene vdW heterostructures. Parts a and b respectively present the top and side views between monolayer MoS_2 and C_{60} heterostructures, part c and d displays side view of the MoS_2/C_{26} and MoS_2/C_{20} heterostructures used in our calculations. Geometry optimizations have first been performed for all of the systems using the conjugate gradient method. The equilibrium distances between fullerene and the top-most atoms of the monolayer MoS_2 are calculated to be 3.04, 2.97 and 3.02 Å for MoS_2/C_{60}, MoS_2/C_{26} and MoS_2/C_{20} (as listed in table 1), which is about equal to those between the GR sheet and other materials (2.65 Å and 2.62 Å for TiO_2(110)/GR [48], 2.85 Å for TiO_2(001)/GR [49, 50], 2.42-2.87 Å for ZnO(0001)/GR[51], 3.32 Å MoS_2/GR [52]). The smaller distance shows that the interaction between monolayer MoS_2 and C_{26} is stronger than that between monolayer MoS_2 and C_{60} (C_{20}). After optimization, the MoS_2 and fullerene are nearly unchanged, indicating that the monolayer MoS_2/fullerene interaction is indeed vdW rather than covalent, in accordance with the others' results [50]. Closer inspection of the atomic position at the interface reveals that, due to the interface interaction between MoS_2 and fullerene, the top-most S atoms are pushed upward about 0.005 and 0.006 Å by C_{60} and C_{20}, respectively; whereas the Mo atoms move upward about 0.001 and 0.004 Å. In the MoS_2/C_{26} heterostructures, however, the corresponding S and Mo atoms move about 0.018 Å. It is indicates that the interaction of MoS_2/C_{26} heterostructures is stronger. The displacement discrepancy of the atoms in the top layer of MoS_2 demonstrates that the interface interaction depends on the carbon number of fullerene.

The rearrangements of atoms in the monolayer MoS_2 indicate that the electron transfer occurs at the interface, which will be discussed later.

The stability of the monolayer MoS_2/fullerene heterostructures can be assessed by the interface adhesion energy, which is defined as

$$E_{ad} = E_{comb} - E_{fullerene} - E_{MoS_2} \tag{3}$$

where E_{comb}, $E_{fullerene}$, and E_{MoS_2} represent the total energy of the relaxed monolayer MoS_2/fullerene, pure fullerene, and pure MoS_2, respectively. By this definition, negative E_{ad} suggests that the adsorption is stable. The interface adhesion energy is calculated to be -1.77, -0.99 and -0.76 eV for the MoS_2/C_{60}, MoS_2/C_{26} and MoS_2/C_{20} heterostructures, respectively, which indicates a rather strong interaction between monolayer MoS_2 and fullerene heterostructures, and the high thermodynamically stability of these heterostructures. Compared with the MoS_2/C_{20} (C_{26}) heterostructures, the MoS_2/C_{60} heterostructures with lower adhesion energy can form more easily.

3.2. Density of States

To explore the effect of vdW interaction on the electronic properties of MoS_2, we have calculated the density of states (DOSs) of individual MoS_2, fullerene, and their heterostructures, as shown in Figure 2. Pure monolayer MoS_2 is a direct semiconductor with a band gap (E_g) of 1.89 eV, which agrees well with the MoS_2 photoluminescence experiment and previous theoretical studies (~1.9 eV) [53]. The CB bottom of pure MoS_2 (Figure 2(a1)) is mainly constituted of Mo 4d and S 3d states, while the upper VB is composed of Mo 4d states. This is one of the most important factors for the lower photocatalytic properties of pure MoS_2. The calculated DOSs show that energy gaps for individual C_{60} and C_{26} are 1.61 and 1.64 eV, respectively (Figures 2 (a2-a4)), which are consistent with other theoretical values of 1.6-1.9 [54] and 1.6 [39] eV, respectively. Interestingly, the energy gap for individual C_{20} is 1.90 eV, in agreement with the value of 1.94 eV with using hybrid B3LYP functional calculations[38], and 1.95 eV with B3LYP/6-31G density functional level of theory calculations[55]. Therefore, the LDA method is also effective method to correctly characterize the electronic structures of the specific MoS_2 monolayer and C_{20} fullerene.

The calculated DOSs of the above four heterostructures characterize the interface electronic properties and energy levels alignment in detail, as shown in Figures 2 (b1)-(b3) and Table 1. One can see that the each component of the combined DOS changes slightly compared to the individual DOSs (Figures 2 (a1)-(a4)), indicating that the interface interaction between monolayer MoS_2 and fullerene is indeed weak. The calculated band gaps of four heterostructures are 1.75, 0.41, and 0.85 eV, respectively, as listed in Table 1. The reduced band gaps can make the heterostructures absorb the most sunlight, and the photogenerated electron transfer from the valence band (VB) to the conduction band (CB) of the monolayer MoS_2/fullerene heterostructures becomes easier. Interestingly, the CB bottom is only consisted of states from C_{60} (C_{26}, C_{20}) which greatly broadens the CB bottom of the monolayer MoS_2/fullerene heterostructures. It should be specially mentioned that when the band gap of C_{60} is 5.08eV (using GW approximations [56]), the CB bottom of MoS_2/C_{60} heterostructure is only consisted of states from MoS_2, thus forming a type-II staggered band alignment, which is in favor of the separation of photogenerated electron-hole pairs. However, the upper part of VB of the monolayer MoS_2/fullerene heterostructures shows complex types. For the MoS_2/C_{20} heterostructures, the upper part of VB is formed from Mo 4d orbits, which can be more clearly seen from the electron density distributions of the highest occupied and lowest unoccupied levels (HOL and LUL), respectively, as shown in Figure 3. More importantly, the MoS_2/C_{20} heterostructures is type II (see Figures 3c), namely, with both the valence and conduction band edges of C_{20} below the corresponding MoS_2 counterparts, which significantly lowers the effective band gap of the heterostructures and facilitates efficient electron-hole separation. Figures 3 (a) clearly displays that the HOL is only composed of the C 2p orbits, while (b) is compose of the Mo 4d, mixing with small S 3p orbits. In photocatalysis, such band alignment is not beneficial for the separation of electron-hole pairs. Thus, the fullerene (C_{20}) would be a sensitizer for MoS_2. These results indicate that choosing appropriate fullerene (such as C_{20}) is especially critical to obtain high efficiency of electron-hole separation in the monolayer MoS_2/fullerene heterostructures.

3.2. Charge Density Difference and Mechanism Analysis

The interaction between MoS_2 and fullerene implies a substantial charge transfer between the involved constituents. This can be visualized (as shown in Figure 4) by three-dimensional charge density difference $\Delta\rho = \rho_{MoS_2/fullerene} - \rho_{MoS_2} - \rho_{fullerene}$, where $\rho_{MoS_2/fullerene}$, ρ_{MoS_2} and $\rho_{fullerene}$ are the charge densities of the heterostructures, the monolayer MoS_2 and fullerene in the same configuration, respectively. Due to the interaction, a very interesting charge redistribution at the monolayer MoS_2/fullerene heterostructures can be obviously observed, which is quite different from those of TiO_2/GR and Ag_3PO_4(100)/GR heterostructures [57, 58]. A strong charge accumulation (green part in Figure 4), mainly from the bottom-most C atoms of the fullerene and some from the charge loosed by S atoms along the *z* axis just under the C atom rings, is found just above the top-most S atoms. Moreover, the charge redistribution at the bottom-most C atoms and the top-most S atoms becomes more significant as the carbon number is decreased (comparing Figures 4(a) with (d)), which is consistent with the shorter interface distance and stronger interaction. Note that the electron losses of different C atoms in the bottom-most and of different S atoms vary with their positions, owing to the different atomic arrangement. Most importantly, closer inspection to Figure 4(d) reveals that the slightly interaction results into the negatively charged Mo atoms in the monolayer MoS_2. This indicates that some Mo atoms at basal planes, initially catalytically inert, would turn out to be active sites, which are beneficial to the improved photocatalytic performance of the monolayer MoS_2/fullerene heterostructures.

To further analyze the charge transfer, part e of Figure 4 plots the planar averaged charge density difference along the direction perpendicular to the MoS_2, which offers quantitative results of charge redistribution. The positive values represent electron accumulation, and negative values indicate electron depletion. It is clear that the largest efficient electron accumulation localized above the top-most S atoms is about 0.90×10^{-4} e/$Å^3$ in the MoS_2/C_{60} heterostructures, the largest local efficient electron depletion at the bottom-most C atoms is about -0.38×10^{-4} e/$Å^3$, while in the $MoS_2/C_{26}(C_{20})$ heterostructures, the largest efficient electron accumulation localized above the top-most C atoms is about 0.68×10^{-4} e/$Å^3$(1.02×10^{-4} e/$Å^3$), and the largest local efficient electron depletion at the bottom-most S atoms is about -1.0×10^{-4} e/$Å^3$ (-0.53×10^{-4} e/$Å^3$). This indicates that the charge transfer is related to the interface distance or vdW interaction.

To quantitatively analyze the charge variation at the interface, the Mulliken population analysis of the plane-wave pseudopotential calculations has been performed on the fullerene, isolated monolayer MoS_2, and monolayer MoS_2/fullerene heterostructures. Figure 5 shows the results of the Mulliken charge on different atoms, in which several typical values are presented. For the isolated monolayer MoS_2, the S and Mo atoms have a Mulliken charge of 0.01 and -0.02, respectively. The interfacial interaction leads to a markedly change of Mulliken charge of each atom in the MoS_2 of the heterostructures, while the Mo atoms become -0.03, -0.02, and -0.01 in the MoS_2/C_{60}, MoS_2/C_{26} and MoS_2/C_{20} heterostructures, respectively, indicating that the electron of Mo atoms of monolayer MoS_2 is reduced due to the coupling of fullerene. The top-most S atoms of monolayer MoS_2 have a Mulliken charge of 0.01, 0.03 (MoS_2/C_{60}), 0.02, 0.03 ($MoS_2/C_{26,}$ MoS_2/C_{20}), respectively. The charge variation demonstrates that the top-most S atoms of the MoS_2/C_{26} (C_{20}) heterostructures would lose more electrons than those in isolated monolayer MoS_2. This would improve the stability of monolayer MoS_2/fullerene photocatalyst, just as the case of MoS_2/GR [52, 59]. Although the C atom in the fullerene has a Mulliken charge of approach zero electrons, those C atoms in the MoS_2/fullerene heterostructures have different Mulliken charges because not only the arrangement of atoms under various C atoms is different, but also the interface interaction is varied. For example, Figure 5(b) shows that, in the MoS_2/C_{60} heterostructures, the C atom has a Mulliken charge of -0.02. Those C atoms at the corresponding to positions in the MoS_2/C_{26} heterostructures have a Mulliken charge of -0.04, -0.02, and 0.01, respectively, it is similar to the case of MoS_2/C_{20} heterostructures. As a result, the charge distribution fluctuations appear at the bottom-most C atoms due to the interactions between monolayer MoS_2 and fullerene.

The effective net charge from one constituent to another in these composites can be analyzed on the basis of the Bader method, as listed in Table 1. The effective net charge from one constituent to another in these heterostructures can be analyzed on the basis of the Bader method, as listed in Table 1. Some electrons transfer from C_{20} (C_{60}) to MoS_2 in the MoS_2/ C_{20} (C_{60}) heterostructures, but it is in the opposite direction in the MoS_2/C_{26} heterostructures. Moreover, the number of electrons transferred from C_{20} to MoS_2 is larger than that from MoS_2 to C_{26} (or from C_{60} to MoS_2). For example, 0.04 (0.007) electron transfers from C_{20} to MoS_2, whereas 0.01 from MoS_2 to C_{26}. To understand the origin of such an interface electron transfer in these heterostructures, work functions for the fullerene and monolayer MoS_2 are calculated by aligning the Fermi level relative to the vacuum energy level. They are calculated to be 4.5, 5.58, 4.45, and

5.35 eV for C_{60}, C_{26}, C_{20}, and monolayer MoS_2, respectively. The spontaneous interfacial charge transfer in the monolayer MoS_2/fullerene heterostructures can be simply rationalized in terms of the difference of these work functions. Moreover, the larger difference in work functions, the more charge transfer. For instance, the work function difference (0.8 eV) between C_{20} and monolayer MoS_2 is larger than that (0.75 (0.23) eV) between C_{60} (C_{26}) and monolayer MoS_2; thus, the transfer amount of charge in the former is bigger than in the former (0.04 vs 0.007(0.01)).

The interface charge redistribution would surely alter the electrostatic potential distribution in whole system. To conduct quantitative analysis, the profile of the planar averaged self-consistent electrostatic potential for the monolayer MoS_2/fullerene heterostructures as a function of position in the z-direction is displayed in Figure 4(c). Surprisingly, the electrostatic potential at the middle region of the interface is close to zero, due to charge redistribution. One can see that the monolayer MoS_2 is a typical S-Mo-S sandwich structure. The potential at the Mo atomic plane is higher than that at the fullerene, resulting into a large potential difference between the two constituents. The built-in potential would be one of the important factors for improving the photocatalytic activity and stability of monolayer MoS_2/fullerene photocatalyst. Under light irradiation, the separation and migration of photogenerated carriers at the interface will be affected by this built-in potential, i.e., the existence of a potential well can effectively hinder the recombination of photogenerated charge carriers in the monolayer MoS_2/fullerene heterostructures. Therefore, the photocatalytic activity and stability of MoS_2 photocatalyst could be improved by coupling fullerene.

3.3. Optical Properties and Photocatalytic Water Splitting

For many semiconductors (for example, TiO_2[6, 60], CeO_2[46], $SrTiO_3$[47], Ag_3PO_4[61], and $g\text{-}C_3N_4$[62]) with wide band gap, the incorporated GR sheet can extend their absorption edge to the vis-light region. Similarly, coupling fullerene with wide-band-gap semiconductors is also an effective strategy to extend the absorption edge and enhance the photocatalytic activity. To explore the influence of the coupled fullerene on the light absorption and photocatalytic performance of MoS_2, the imaginary part of the dielectric function and UV-vis absorption spectra of monolayer MoS_2 and the monolayer MoS_2/fullerene heterostructures are calculated, as shown in Figure 6. For the momolayer MoS_2, the optical absorption occurs at about 1.89 eV [44], which is attributed to the intrinsic transition from the Mo 4d to S 3p orbitals. As can be clearly seen from Figure 6, the absorption intensity of MoS_2/fullerene heterostructures is enhanced significantly in the UV-vis light region. Miraculously the shape of absorption curve of the monolayer MoS_2/fullerene heterostructures depends on the carbon number of the fullerene (see Figure 6(b)), indicating that the electronic transitions are different. In the region from 400 to 420 nm, the absorption of MoS_2/C_{60} heterostructures is much higher than that of MoS_2/C_{26} (C_{20}) heterostructures; whereas for the latter, interestingly, in the region from 530 to 700 nm, the absorption is much higher than that of MoS_2/C_{60} heterostructures. These distinctions can be attributed to the difference of electronic structures, especially those near the band gap (Figures 2 and 3). Thus, it is reasonable to conclude that coupling fullerene on the MoS_2 semiconductor would lead to the enhanced absorption in the UV-vis region, which is one of the most important factors to improve the photocatalytic activity of MoS_2.

It is well known that the enhanced photocatalytic activity mainly derives from the efficient generation, separation and transfer process of the photoinduced electron–hole pairs, which strongly depends on the band structure of the composite photocatalyst. The redox ability of MoS_2/C_{26} (C_{20}) heterostructures is assessed by determining the energy positions of valence and conduction bands with respect to the water oxidation/reduction potential level. However, the band edge energies of the CB could not be determined directly by electrochemical analysis. To give direct analysis, the CBM and VBM of MoS_2/C_{20} compound can be estimated from the absolute electronegativity of the atoms and the band gap of the semiconductors by the following equations [63, 64]:

$$E_{VB} = X - E_e + 0.5E_g \tag{4}$$

$$E_{CB} = E_{VB} + E_g \tag{5}$$

Here E_{VB} and E_{CB} are the VB and CB edge potentials, X is the electronegativity of the semiconductor (the geometric mean of the electronegativities of the constituent atoms), E_e is the standard electrode potential on the hydrogen scale (~4.5 eV), and E_g is the band gap. The X values for monolayer MoS_2 and C_{20} were 5.324 and 6.27 eV, respectively.

Figure 7 displays the charge transfer pathway of the MoS_2/C_{20} heterostructures under visible light irradiation. Clearly, the interactive band structure of the MoS_2/C_{20} is favorable for the transfer of photogenerated charge carriers. The photoinduced electrons can transfer easily from the CB bottom of MoS_2 to that of C_{20}, while the holes left on the VB top of C_{20} move in the opposite direction to the VB top of MoS_2. Thus, the photoinduced electrons and holes are separated efficiently, resulting in enhanced photocatalytic activity. Furthermore, the calculated VB and CB edge potentials are also shown in Figure 7. In the monolayer MoS_2 the CB edge potential is -0.12 V, which is lower than that of H^+/H_2 (0 eV), and the VB edge potential is 1.77 eV, which is higher than that of O_2/H_2O (1.23 V). Therefore, the monolayer MoS_2 has the ability to oxidize H_2O to produce O_2 or oxidation pollutants and can reduce H^+ to H_2. The calculations consistent with theoretical results [65, 66]. Whereas, in the MoS_2/C_{20} heterostructures, the VB edge potential is 1.674 eV, the CB edge potential is 0.82 eV. Therefore, the MoS_2/C_{20} heterostructures has the ability to oxidize H_2O to produce O_2 or oxidation pollutants but cannot reduce H^+ to H_2. This indicates that the MoS_2/C_{20} heterostructure would be a potential substitute for these expensive metal oxide photocatalysts, such as Ag_3PO_4 [67], to harness visible light to oxidize water as well as decompose organic contaminants.

4. Summary

In summary, using first-principles DFT calculations, we have studied changes in the electronic structure, charge transfer and photoactivity activity of MoS_2 in the presence of various non-covalently bound fullerenes. It is unveiled that the fullerene C_{20} can act as a sensitizer in MoS_2 nanocomposites to improve the photocatalytic activity. Compared to monolayer MoS_2, the monolayer MoS_2/fullerene heterostructures has a smaller band gap (1.75, 0.41 and 0.85 eV), thus extending the absorption spectrum covering the entire visible region. The type-II, staggered, band alignment existing between monolayer MoS_2 and C_{20} can promote the separation of photoinduced carriers, thus enhancing the photocatalytic activity. It is expected that C_{20} acts as a sensitizer in other fullerene-MoS_2 nanocomposites. This strongly suggests possible applications in photocatalysis. These findings provide a theoretical basis for developing highly efficient MoS_2-based or fullerene-based photocatalysts.

Acknowledgements

This work was supported by the National Natural Science Foundation of China (Grant Nos. 51471068 and 51271075).

References

1. R. Asahi, T. Morikawa, T. Ohwaki, K. Aoki and Y. Taga, *Science*, 2001, **293**, 269-271.
2. X. Chen and S. S. Mao, *Chemical Reviews*, 2007, **107**, 2891-2959.
3. Z. G. Zou, J. H. Ye, K. Sayama and H. Arakawa, *Nature*, 2001, **414**, 625-627.
4. M. Ni, M. K. H. Leung, D. Y. C. Leung and K. Sumathy, *Renewable and Sustainable Energy Reviews*, 2007, **11**, 401-425.
5. T. L. Thompson and J. T. J. Yates, *Chemical Reviews*, 2006, **106**, 4428-4453.
6. J. W. Sha, N. Q. Zhao, E. Z. Liu, C. S. Shi, C. C. He and J. J. Li, *Carbon*, 2014, **68**, 352-359.
7. M. Q. Yang, N. Zhang and Y. J. Xu, *ACS Applied Materials & Interfaces*, 2013, **5**, 1156-1164.
8. P. Kumar, H. P. Mungse, S. Cordier, R. Boukherroub, O. P. Khatri and S. L. Jain, *Carbon*, 2015, **94**, 91-100.
9. L. Xu, W. Q. Huang, L. L. Wang, Z. A. Tian, W. Y. Hu, Y. M. Ma, X. Wang, A. L. Pan and G. F. Huang, *Chemistry of Materials*, 2015, **27**, 1612-1621.
10. J. G. Yu, S. H. Wang, J. X. Low and W. Xiao, *Physical Chemistry Chemical Physics*, 2013, **15**, 16883-16890.
11. Y. H. Zhang, Z. R. Tang, X. Z. Fu and Y. J. Xu, *ACS Nano*, 2011, **5**, 7426-7435.
12. D. M. Poirier, T. R. Ohno, G. H. Kroll, Y. Chen, P. J. Benning, J. H. Weaver, L. P. F. Chibante and R. E. Smalley, *Science*, 1991, **253**, 646-648.
13. Q. Liu, Y. R. Guo, Z. H. Chen, Z. G. Zhang and X. M. Fang, *Applied Catalysis B: Environmental*, 2016, **183**, 231-241.

14. A. J. Du, Y. H. Ng, N. J. Bell, Z. H. Zhu, R. Amal and S. C. Smith, *Journal of Physical Chemistry Letters*, 2011, **2**, 894-899.

15. Q. J. Xiang, J. G. Yu and M. Jaroniec, Journal of Physical Chemistry C, 2011, **115**, 7355-7363.

16. W. K Jo, T. Adinaveen, J. J. Vijaya and N.C.S. Selvam, *RSC Advances*, 2016, **6**, 10487-10497.

17. J.Z Ma, C. X. Wang and H. He, *Applied Catalysis B: Environmental*, 2016, **184**, 28-34.

18. V. Apostolopoulou, J. Vakros, C. Kordulis and A. Lycourghiotis, *Colloids and Surfaces A: Physicochemical and Engineering Aspects*, 2009, **349**, 189-194.

19. L. Y. Gan, Q. Zhang, Y. Cheng and U. Schwingenschlogl, *Journal of Physical Chemistry Letters*, 2014, **5**, 1445-1449.

20. X. Q. An and J. C. Yu, *RSC Advances*, 2011, **1**, 1426.

21. X. W. Cheng, H. L. Liu, Q. H. Chen, J. J. Li and P. Wang, *Carbon*, 2014, **66**, 450-458.

22. Y. M. Shi, W. Zhou, A. Y. Lu, W. J. Fang, Y. H. Lee, A. L. Hsu, S. M. Kim, K. K. Kim, H. Y. Yang, L. J. Li, J. C. Idrobo and J. Kong, *Nano Letters*, 2012, **12**, 2784-2791.

23. H. Rydberg, M. Dion, N. Jacobson, E. Schroder, P. Hyldgaard, S. I. Simak, D. C. Langreth and B. I. Lundqvist, *Biophysical Reviews and Letters*, 2003, **91**, 126402.

24. A. L. Walter, H. Sahin, K.-J. Jeon, A. Bostwick, S. Horzum, R. Koch, F. Speck, M. Ostler, P. Nagel and M. Merz, *ACS nano*, 2014, **8**, 7801-7808.

25. J. Chen, S. L. Li and Z. L. Tao, *Journal of Alloys and Compounds*, 2003, **356**, 413-417.

26. X. L. Wei, H. Zhang, G. C. Guo, X. B. Li, W. M. Lau and L. M. Liu, *Journal of Materials Chemistry A*, 2014, **2**, 2101-2109.

27. J. Xu and X. J. Cao, *Biochemical Engineering Journal*, 2015, **260**, 642-648.

28. Y. Y. Zhu, Q. Ling, Y. F. Liu, H. Wang and Y. F. Zhu, *Physical Chemistry Chemical Physics*, 2015, **17**, 933-940.

29. J. Z. Li, K. Yu, Y. H. Tan, H. Fu, Q. F. Zhang, W. T. Cong, C. Q. Song, H. H. Yin and Z. G. Zhu, *Dalton Transactions*, 2014, **43**, 13136-13144.

30. Y. Song, Y. Lei, H. Xu, C. Wang, J. Yan, H. Zhao, Y. Xu, J. Xia, S. Yin and H. Li, *Dalton Transactions*, 2015, **44**, 3057-3066.

31. Y. L. Yuan, X. P. Gong and H. M. Wang, Physical Chemistry Chemical Physics, 2015, **17**, 11375-11381.

32. V. O. Koroteev, L. G. Bulusheva, I. P. Asanov, E. V. Shlyakhova, D. V. Vyalikh and A. V. Okotrub, *Journal of Physical Chemistry C*, 2011, **115**, 21199-21204.

33. K. H. Lee, J. Y. Lee and Y. G. Hwang, *Bulletin of the Korean Chemical Society*, 2013, **34**, 365-366.

34. M. Q. Yang, N. Zhang and Y. J. Xu, *ACS Applied Materials & Interfaces*, 2013, **5**, 1156-1164.

35. L. E. Ratcliff and P. D. Haynes, *Physical Chemistry Chemical Physics*, 2013, **15**, 13024-13031.

36. A. K. Pandey and J. M. Nunzi, *Advanced Materials*, 2007, **19**, 3613-3617.

37. H. B. Fu, T. G. Xu, S. B. Zhu and Y. F. Zhu, *African Journal of Environmental Science and Technology*, 2008, **42**, 8064-8069.

38. Y. Cao, D. W. Wang, B. Liu, G. J. Yao, Y. T. Fu, X. J. Li and Z. G. Bi, International Journal of Quantum Chemistry, 2013, **113**, 1440-1446.

39. J. An, L. H. Gan, J. Q. Zhao and R. Li, *Chinese Journal of Chemical Physics*, 2010, **132**, 154304.

40. X. J. Bai, L. Wang, Y. J. Wang, W. Q. Yao and Y. F. Zhu, *Applied Catalysis B: Environmental*, 2014, **152-153**, 262-270.

41. M. Remskar, A. Mrzel, A. Jesih, J. Kovac, H. Cohen, R. Sanjines and F. Levy, *Advanced Materials*, 2005, **17**, 911-914.

42. V. Hakkim and S. Biplab, *RSC Advances*, 2015, **10**, 1039.

43. O. Leenaerts, B. Partoens and F. M. Peeters, *Applied Physics Letters*, 2008, **92**, 243125.

44. E. Ridolfi, D. Le, T. S. Rahman, E. R. Mucciolo, and C. H. Lewenkopf, *Journal of Physics: Condensed Matter,* 2015, **27**, 365501.

45. H. Wan, L. Xu, W. Q. Huang, J. H. Zhou, C. N. He, X. F. Li, G. F. Huang, P. Peng and Z. G. Zhou, *RSC Advances*, 2015, **5**, 7944-7952.

46. L. Xu, W. Q. Huang, L. L. Wang and G. F. Huang, *ACS Applied Materials & Interfaces*, 2014, **6**, 20350-20357.

47. Y. C. Yang, L. Xu, W. Q. Huang, C. Y. Luo, G. F. Huang and P. Peng, *Journal of Physical Chemistry C*, 2015, **119**, 19095-19104.

48. X. H. Li, H. T. Gao and G. G. Liu, *Computational and Theoretical Chemistry*, 2013, **1025**, 30-34.

49. P. Zhou, X. F. Zhu, J. G. Yu and W. Xiao, *ACS Applied Materials & Interfaces*, 2013, **5**, 8165-8172.

50. H. T. Gao, X. H. Li, J. Lv and G. J. Liu, *Journal of Physical Chemistry C*, 2013, **117**, 16022-16027.

51. P. T. Xu, Q. X. Tang and Z. Zhou, *Nature Nanotechnology*, 2013, **24**, 305401.

52. W. Y. Zan, W. Geng, H. X. Liu and X. J. Yao, *Nature Nanotechnology*, 2015, **649**, 961-967.

53. K. F. Mak, C. G. Lee, J. Hone, J. Shan and T. F. Heinz, *Physical Review Letters*, 2010, **105,** 136805.

54. G. K. R. Senadeera and V. P. S. Perera, *Chinese Journal of Physics*, 2004, **43**, 384-390.

55. Z. Chen, J. Cioslowski, N. Rao, D. Moncrieff, M. Bühl, A. Hirsch and W Thiel, *Theoretical Chemisty Accounts,* 2001, **106**, 352-363.

56. X. Blase, C. Attaccalite and V. Olevano, *Physical Review B: Condensed Matter* 2011, **83**, 115103.

57. J. J. Fan, S. W. Liu and J. G. Yu, *Journal of Materials Chemistry*, 2012, **22**, 17027-17036.

58. L. Xu, W. Q. Huang, L. L. Wang, G. F. Huang and P. Peng, *Journal of Materials Chemistry*, 2014, **118**, 12972-12979.

59. Y. Ma, Y. Dai, M. Guo, C. Niu and B. Huang, *Nanoscale*, 2011, **3**, 3883-3887.

60. Y. H. Zhang, Z. R. Tang, X. Z. Fu and Y. J. Xu, *ACS Nano*, 2010, **4**, 7303-7314.

61. Z. M. Yang, G. F. Huang, W. Q. Huang, J. M. Wei, X. G. Yan, Y. Y. Liu, C. Jiao, Z. Wan and A. Pan, *Journal of Materials Chemistry A* 2014, **2**, 1750-1756.

62. D. Ghosh, G. Periyasamy and S. K. Pati, *Journal of Physical Chemistry C*, 2014, **118**, 15487-15494.

63. J. Cao, B. Xu, H. Lin, B. Luo and S. Chen, *Dalton Transactions*, 2012, **41**, 11482-11490.

64. J. Liu, X. Fu, S. Chen and Y. Zhu, *Applied Physics Letters*, 2011, **99**, 191903.

65. N. Singh, G. Jabbour and U. Schwingenschlögl, *The European Physical Journal B*, 2012, **85**, 1-4.

66. J. Kang, S. Tongay, J. Zhou, J. Li and J. Wu, *Applied Physics Letters*, 2013, **102**, 012111.

67. Z. G. Yi, J. H. Ye, N. Kikugawa, T. Kako, S. X. Ouyang, H. Stuart-Williams, H. Yang, J. Y. Cao, W. J. Luo, Z. S. Li, Y. Liu and R. L. Withers, *Nature Materials*, 2010, **9**, 559-564.

Structure	E_{ad} (eV)	E_g (eV)	d (Å)	Bader Charge (e)	
				MoS_2	C
MoS_2/C_{60}	-1.77	1.75	3.04	-0.007	0.007
MoS_2/C_{26}	-0.99	0.41	2.97	0.01	-0.01
MoS_2/C_{20}	-0.76	0.85	3.02	-0.04	0.04

Table 1: The adhesion energy (E_{ad}), band gap E_g(eV), mean distance (d) of optimized MoS_2/C_{60}, MoS_2/C_{26}, and MoS_2/C_{20} heterostructures.

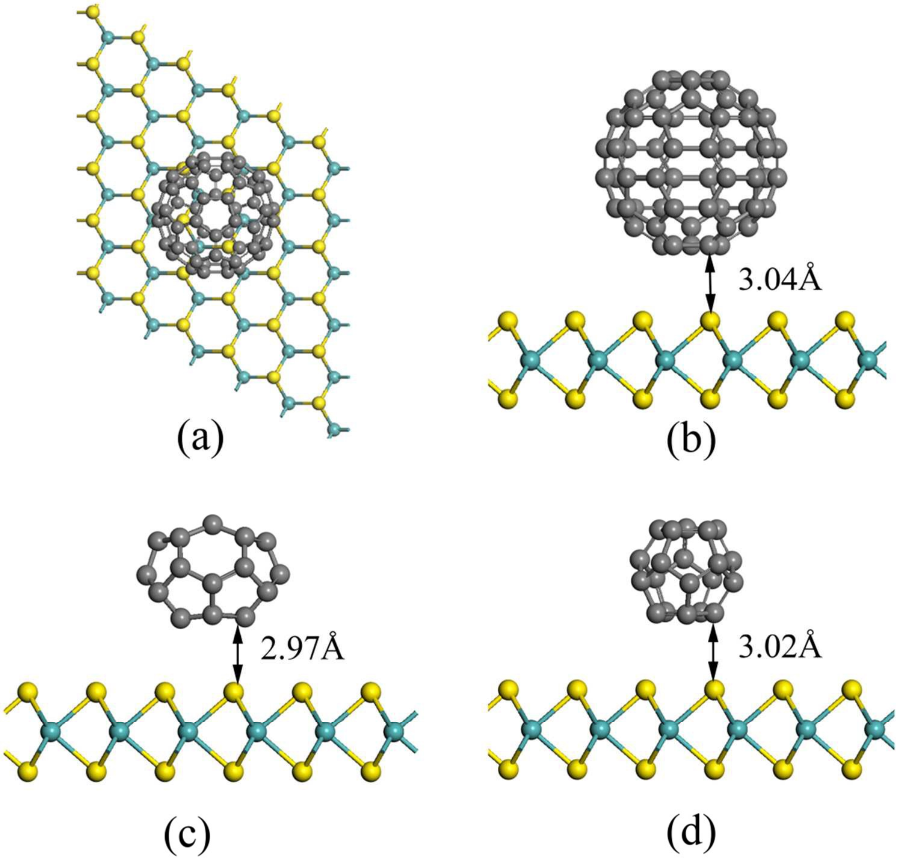

Figure 1: The (a) top and (b) side view of the simulating interface between C_{60} and MoS_2 heterostructures, (c) and (d) side view of the simulating interface between C_{26}, C_{20} and MoS_2 heterostructures. Gray, green and yellow spheres represent C, Mo and S atoms, respectively.

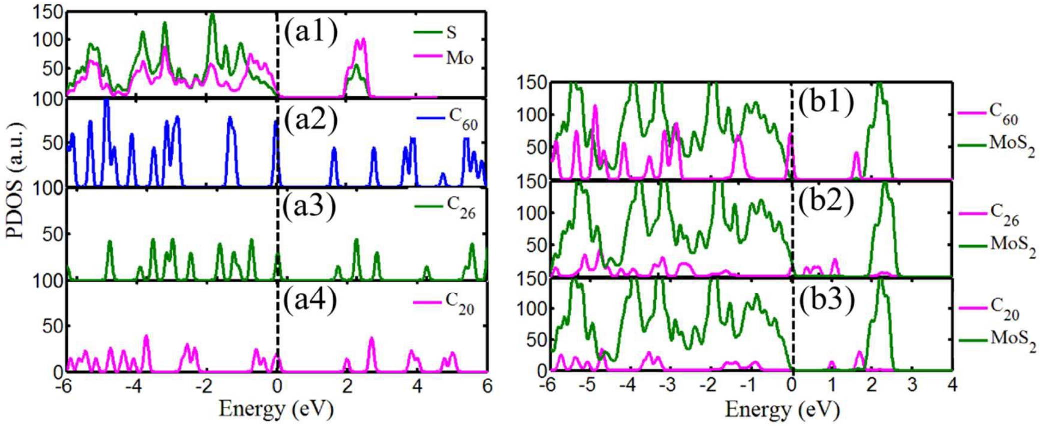

Figure 2: DOS for (a1-a4) pure MoS_2, C_{60}, C_{26}, and C_{20}; (b1-b3) MoS_2/C_{60}, MoS_2/C_{26}, and MoS_2/C_{20}, respectively. The Fermi level is set to zero energy.

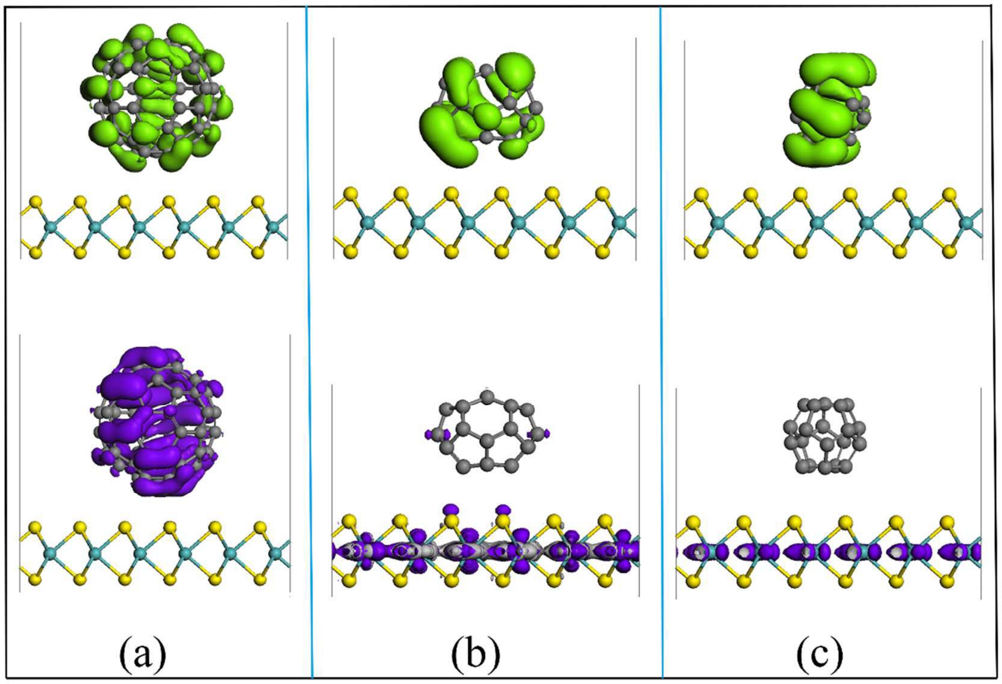

Figure 3: Maps of the charge density distributions of the lowest unoccupied (upper panel) and highest occupied levels (lower panel). (a-c) are for the MoS_2/C_{60}, MoS_2/C_{26}, and MoS_2/C_{20} heterostructures, respectively. The isovalue is 0.006 e/Å^3.

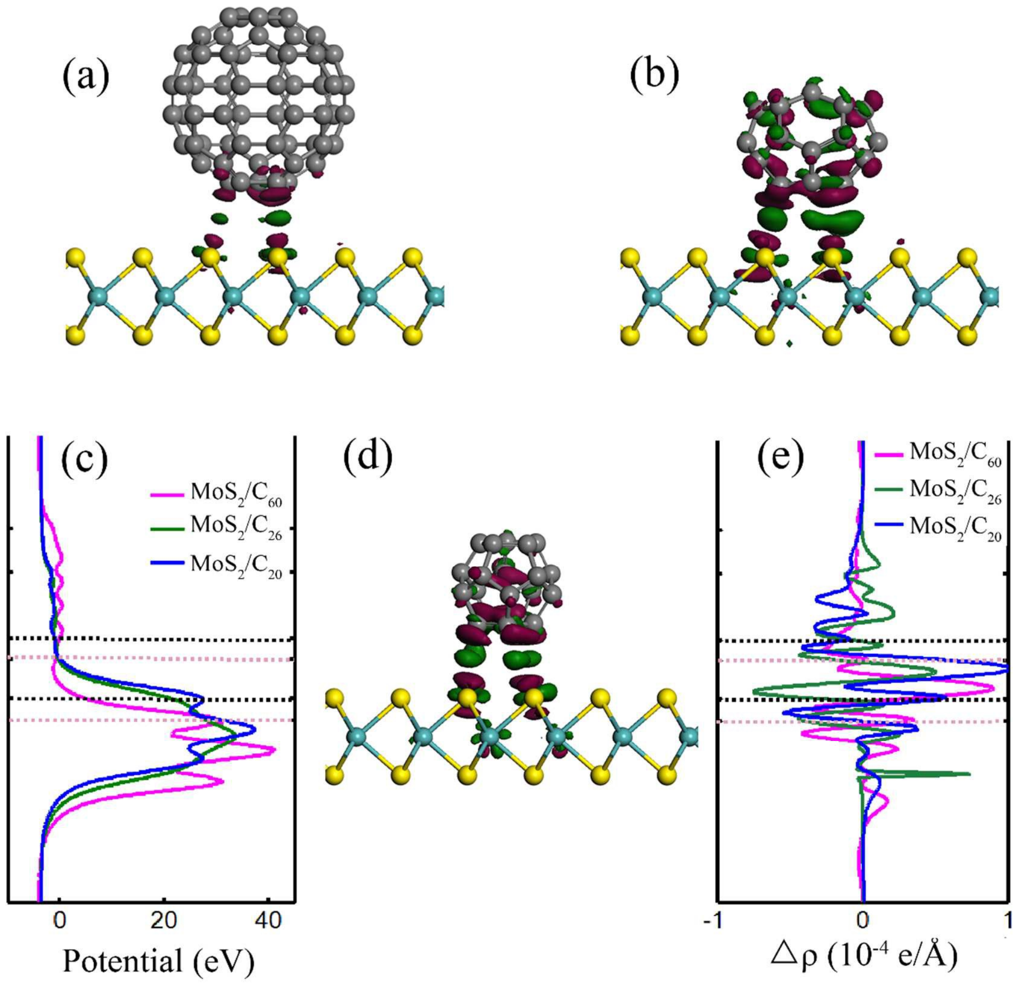

Figure 4: 3D Charge density differences for (a) MoS$_2$/C$_{60}$, (b) MoS$_2$/C$_{26}$, (d) MoS$_2$/C$_{20}$ heterostructures. The green and wine red represent charge accumulation and depletion, respectively. The isovalue is 0.002 e/Å^3. (c) Profile of the planar averaged self-consistent electrostatic potential for the MoS$_2$/C$_{60}$ (C$_{26}$, C$_{20}$) as a function of position in the z-direction. (e) Profile of the planar averaged charge density difference for the MoS$_2$/C$_{60}$ (C$_{26}$, C$_{20}$) as a function of position in the z-direction. The horizontal black (pink) dashed line from up to down indicates the location of the bottom C atoms, the top of the S atoms respectively.

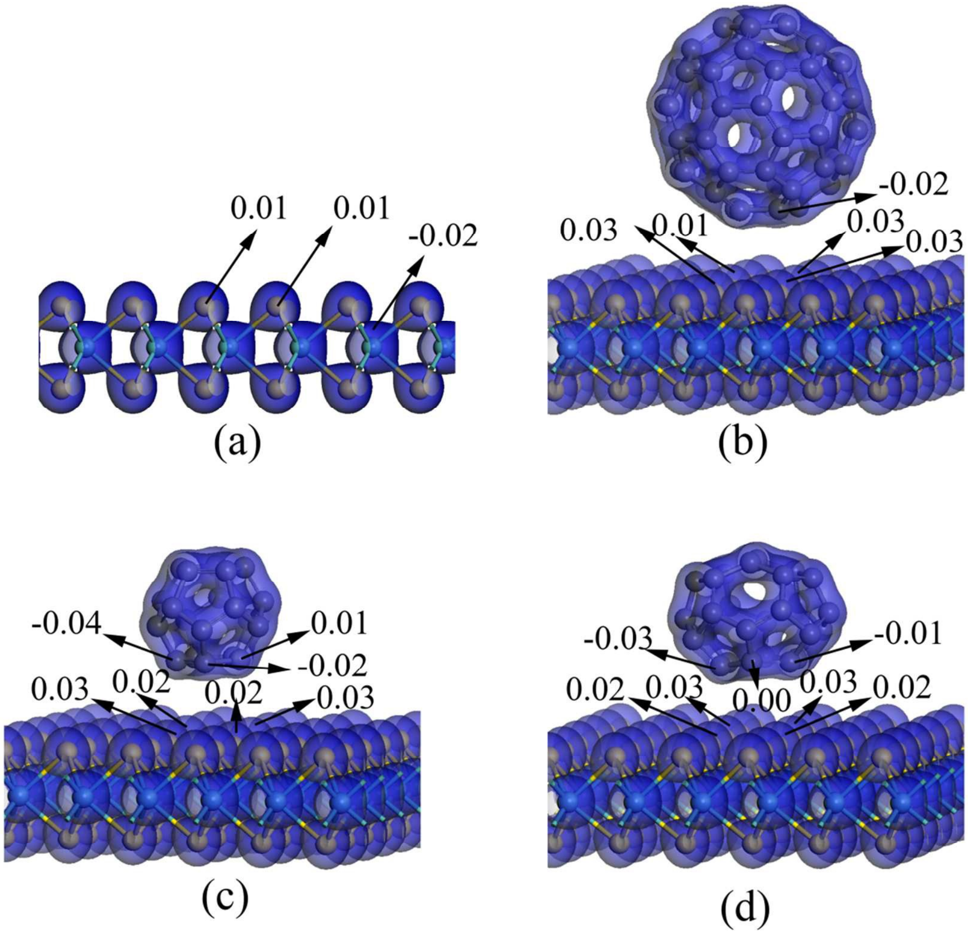

Figure 5. Charge distribution maps of (a) MoS_2, (b) MoS_2/C_{60}, (c) MoS_2/C_{26}, and (d) MoS_2/C_{20}, with an isovalue of 0.7 e/Å^3. Gray, green and yellow spheres represent C, Mo and S atoms, respectively.

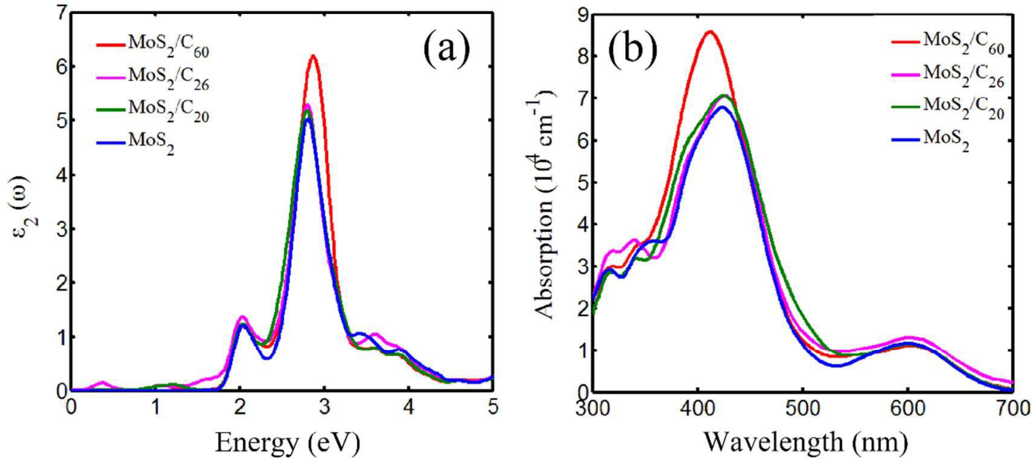

Figure 6: Calculated (a) imaginary part of the dielectric function and (b) absorption spectra of the MoS_2 (blue solid line), MoS_2/C_{60} (red solid line), MoS_2/C_{26} (rose red solid line) and MoS_2/C_{20} (green solid line) heterostructures, respectively.

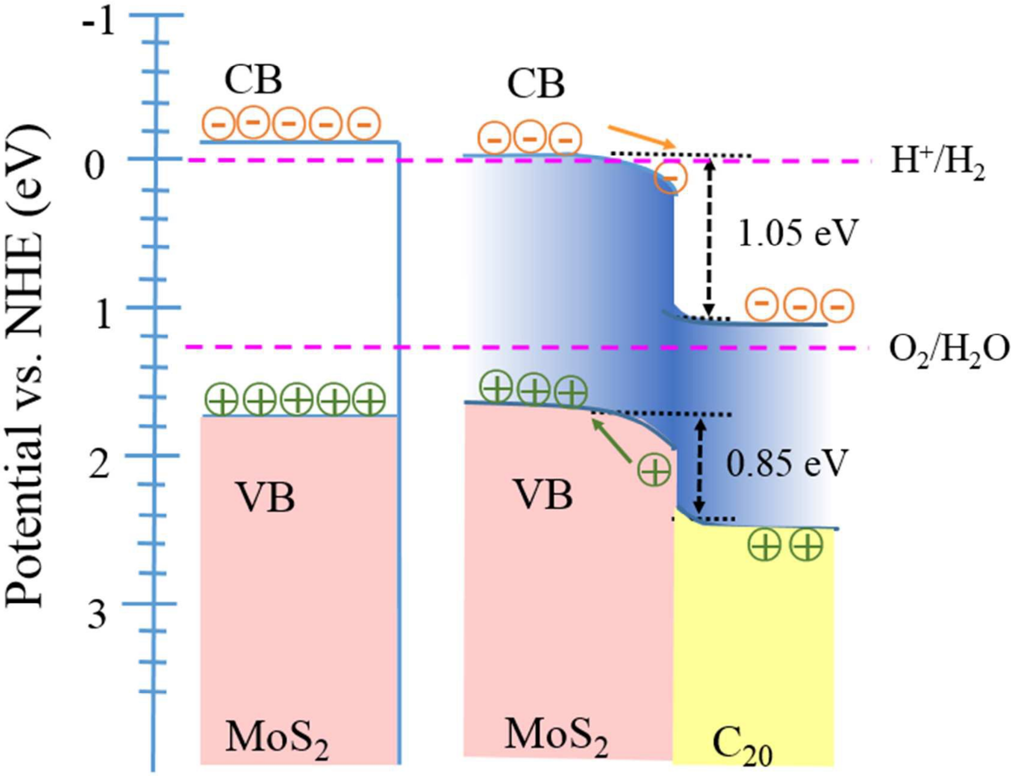

Figure 7. Calculated VB and CB potentials versus normal hydrogen electrode of monolayer MoS_2 and MoS_2/C_{20} heterostructures. The carrier transfer and separation in the MoS_2/C_{20} heterostructures is displayed.

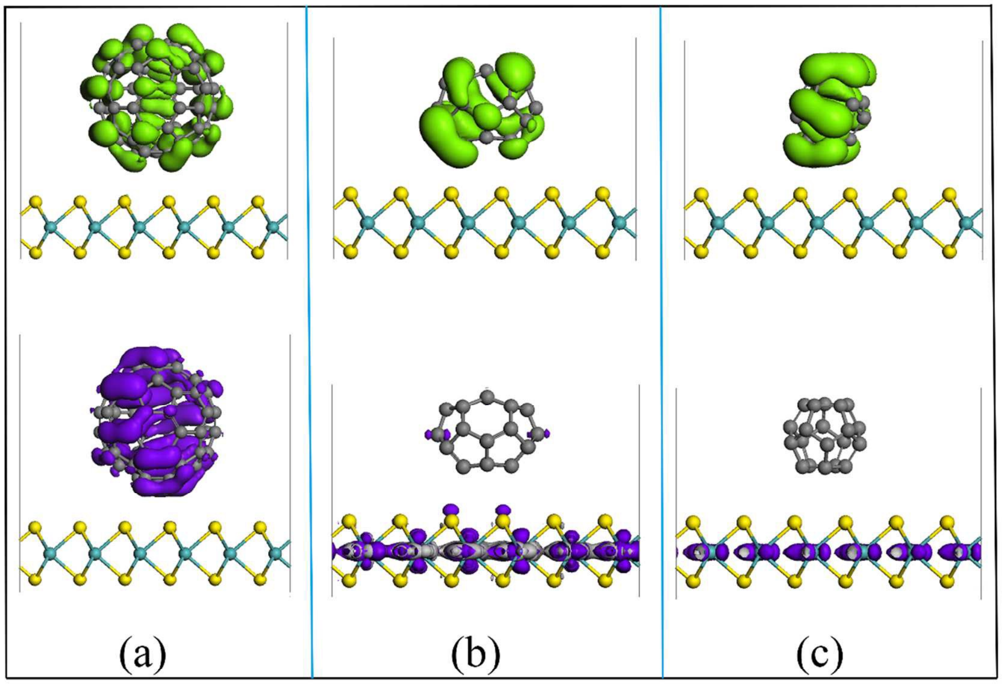

Graphical Abstract